

3D-printed clay components with high surface area for passive indoor moisture buffering

*Original*

3D-printed clay components with high surface area for passive indoor moisture buffering / Gentile, V., Vargas Velasquez, J.D., Fantucci, S., Autretto, G., Gabrieli, R., Gianchandani, P.K., Armandi, M., Bairo, F.. - In: JOURNAL OF BUILDING ENGINEERING. - ISSN 2352-7102. - 91:(2024), pp. 1-13. [10.1016/j.jobe.2024.109631]

*Availability:*

This version is available at: 11583/2989356 since: 2024-06-06T12:29:19Z

*Publisher:*

Elsevier

*Published*

DOI:10.1016/j.jobe.2024.109631

*Terms of use:*

This article is made available under terms and conditions as specified in the corresponding bibliographic description in the repository

*Publisher copyright*

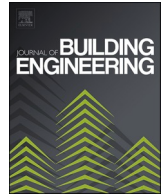
(Article begins on next page)



ELSEVIER

Contents lists available at [ScienceDirect](https://www.sciencedirect.com)

## Journal of Building Engineering

journal homepage: [www.elsevier.com/locate/job](http://www.elsevier.com/locate/job)

## 3D-printed clay components with high surface area for passive indoor moisture buffering

Vincenzo Gentile<sup>a,\*</sup>, Juan Diego Vargas Velasquez<sup>a</sup>, Stefano Fantucci<sup>a</sup>,  
Giorgia Autretto<sup>a</sup>, Roberta Gabrieli<sup>b</sup>, Pardeep Kumar Gianchandani<sup>b,c</sup>,  
Marco Armandi<sup>b</sup>, Francesco Baino<sup>b</sup>

<sup>a</sup> *TEBE Research Group, Department of Energy (DENEG), Politecnico di Torino, 10129, Turin, Italy*

<sup>b</sup> *Institute of Materials Physics and Engineering, Department of Applied Science and Technology (DISAT), Politecnico di Torino, 10129, Turin, Italy*

<sup>c</sup> *Mehran University of Engineering & Technology, Department of Textile Engineering, Jamshoro, 76062, Sindh, Pakistan*

### ARTICLE INFO

#### Keywords:

Moisture buffering  
3D printing  
Clay  
Passive moisture control  
Surface area

### ABSTRACT

This study focuses on implementing a novel approach in which clay 3D-printed matrices were designed as a passive comfort solution to enhance indoor moisture buffering and air quality. Liquid Deposition Modeling additive manufacturing and parametric design were implemented to develop the components, which were characterized for having an increased specific surface exposed to air and moisture per volume unit, which showed to significantly enhance moisture buffering. This revealed a clear linear relationship between the two parameters. Additionally, the components showed a significant increase in the practical Moisture Buffering Value (MBV) and mass reduction compared to a solid clay reference. Furthermore, this research analyzed the influence of two stabilization techniques on the moisture uptake capacity of the samples, i.e. thermal treatment at different temperatures between 600 and 1000 °C and mixing with calcium hydroxide paste within the 10–40 % range. Finally, the morphological (scanning electron microscopy) and crystallographic (X-ray diffraction) analyses of the samples show a correlation between microstructural modifications and the variations of moisture uptake capacity and MBV. In addition, nitrogen adsorption-desorption measurements revealed that sample porosity decreased as the temperature of the thermal treatment increased, showing a correlation with the decrease of practical MBV.

### 1. Introduction

Using building materials as passive moisture regulators represents an environmentally sustainable and energy-efficient strategy for mitigating indoor humidity fluctuations, thus improving indoor environmental quality [1–3].

Typical building materials such as gypsum, lime, wood, clay, and concrete can absorb and retain moisture from the surrounding air. The Moisture Buffer Value (MBV) is a key performance indicator that quantifies the capacity of a material or component to absorb and release moisture under standard room temperature (T) and relative humidity (RH) conditions [4]. Conventional building materials (gypsum [5,6], lime [7,8], wood [9,10], and concrete [11–13]) exhibit moderate MBV values, from 0.6 to 1.5 g/(m<sup>2</sup> %RH) [4,14,15], while some others (paper, textiles, and clay) can potentially reach higher values [4,16].

\* Corresponding author.

E-mail address: [vincenzo.gentile@polito.it](mailto:vincenzo.gentile@polito.it) (V. Gentile).

<https://doi.org/10.1016/j.job.2024.109631>

Received 21 December 2023; Received in revised form 9 May 2024; Accepted 14 May 2024

Available online 17 May 2024

2352-7102/© 2024 The Author(s). Published by Elsevier Ltd. This is an open access article under the CC BY-NC-ND license (<http://creativecommons.org/licenses/by-nc-nd/4.0/>).

Most of the recent research focuses on enhancing the MBV of materials used in indoor walls. This enhancement aims to achieve exceptional MBV values ( $>3 \text{ g}/(\text{m}^2 \text{ \%RH})$ ) to enable passive control of indoor humidity, thus reducing mechanical ventilation and preventing mold growth [15,17,18]. In this sense, numerous studies [6,7,13,19–23] have already demonstrated that incorporating hygroscopic or microporous sorbents in plasters can significantly augment the MBV of materials and composites.

Despite MBV might increase up to 6–15  $\text{g}/(\text{m}^2 \text{ \%RH})$  [24,25] by adding chemicals or aggregates to the plaster recipe, the application at the building scale faces the limitation of having at most 3–4 walls and the ceiling as available surfaces.

At the same time, exploiting the thickness of the absorbing layer has limitations due to the resistance of moisture transport in building materials. Indeed, typical values of the moisture diffusivity are in the order of  $<10^{-10} \text{ m}^2/\text{s}$ , and the mass transfer Biot number is higher than 10 [26]. Consequently, the effective penetration depth of moisture lies in the order of  $10^{-3} \text{ m}$  for daily moisture variations and  $10^{-2} \text{ m}$  on a seasonal scale [27–29]. Using moisture buffering materials with a layer depth thicker than the moisture penetration depth will produce negligible or null effects for indoor moisture control (daily fluctuations). Moreover, this approach can potentially lead to using a large amount of material with no justified environmental impact.

Increasing the available surfaces, for instance, generating geometries more complex than flat surfaces, is a path still underexplored by the scientific academy. Extended surfaces gain the interaction of moisture with the buffering material, proportionally contributing to mass transfer.

In this research, we exploit additive manufacturing to explore the potential of complex geometries in enhancing moisture control using building materials. The benefit is the rational use of materials to improve component functionality and aesthetics with an oriented design of surfaces and structures [30].

3D printing with Liquid Deposition Modeling (LDM) [31–34] is an emerging technique in the building sector for large-scale applications [35–42]. LDM is a printing process in which a fluid/dense material is extruded through a nozzle to construct an object by depositing layers on each other. Unlike other printing techniques, any object manufactured with LDM is sensible to mixture composition and drying or curing operations required for long-term durability. LDM relies on material plasticity, tensile strength, and viscous properties to produce self-supporting structures. Unlike concrete, gypsum, or lime, clay has mechanical and viscous properties fitting the technological constraints of this technology [31,43–47].

In addition, unfired clay exhibits favorable hygroscopic properties for indoor moisture buffering and the possibility of exploiting natural resources locally. Clay performs better buffering than conventional building materials, with MBV between 1.5 and 4  $\text{g}/(\text{m}^2 \text{ \%RH})$  [16]. However, it requires stabilization to guarantee long-term, safe usage. The application of molded products made from dried clay is practically impossible due to the low strength of clay samples in the dried state and the loss of integrity with the transition to plastic mass upon direct contact with water.

Various stabilization methods and techniques can prevent erosion and cracking of clay artifacts based on mechanical, chemical, and thermal treatments. Only the last two are suitable for clay 3D-printed objects based on LDM techniques. For example, applying a thermal treatment with oven temperatures set up to 900–1000 °C reduces the apparent porosity and increases the indirect tensile strength to 5–8 MPa [48,49]. On the other hand, including some mineral activators in the clay/water composition may lead to similar results with reduced environmental impact [50–52]. In both cases, equilibrium moisture uptake and related transport properties may change.

Complex geometries generated by the 3D printing of clay have found interesting applications in multiple sectors and for different goals, e.g., enhancing heat transfer [53] and heat storage [54] or functionalized bricks with enhanced thermal [44,45,55] and hygroscopic [36] properties.

However, printing complex shapes generates issues related to the feasibility of the geometry and long printing durations [56]. For example, gyroid geometries are triply periodic minimal surfaces with a very high surface area-to-volume ratio requiring high-resolution constraints (2 mm extruder nozzle and 1 mm printing layer height) as well as relatively long printing time (higher than 4 h) [57,58].

This research work focuses on two main objectives. The first is to produce indoor components with complex geometries and increased surface areas to enhance their moisture buffering properties, measured by assessing the practical MBV value. The second is to compare the impact of two different stabilizing procedures on the component hygroscopic performance (thermal versus chemical clay treatment). Although this research uses a conventional material (clay) and well-established additive manufacturing technologies, the novelty relies on the combination of both and the final goal: in fact, there are very few previous publications in the literature dealing with the application of 3D printing in exploiting geometrical complexity to address indoor moisture buffering [30].

## 2. Methodology

The research methodology followed an experimental approach combining materials science, computational design, additive manufacturing, and laboratory assessment. Firstly, to fully leverage clay moisture absorption capabilities, the component design pursued the strategy of increasing surface exposure to the indoor environment. The result was a prototype of a cladding-wall component with complex geometrical features generated using parametric and algorithmic design strategies with *Grasshopper* for *Rhinoceros*.

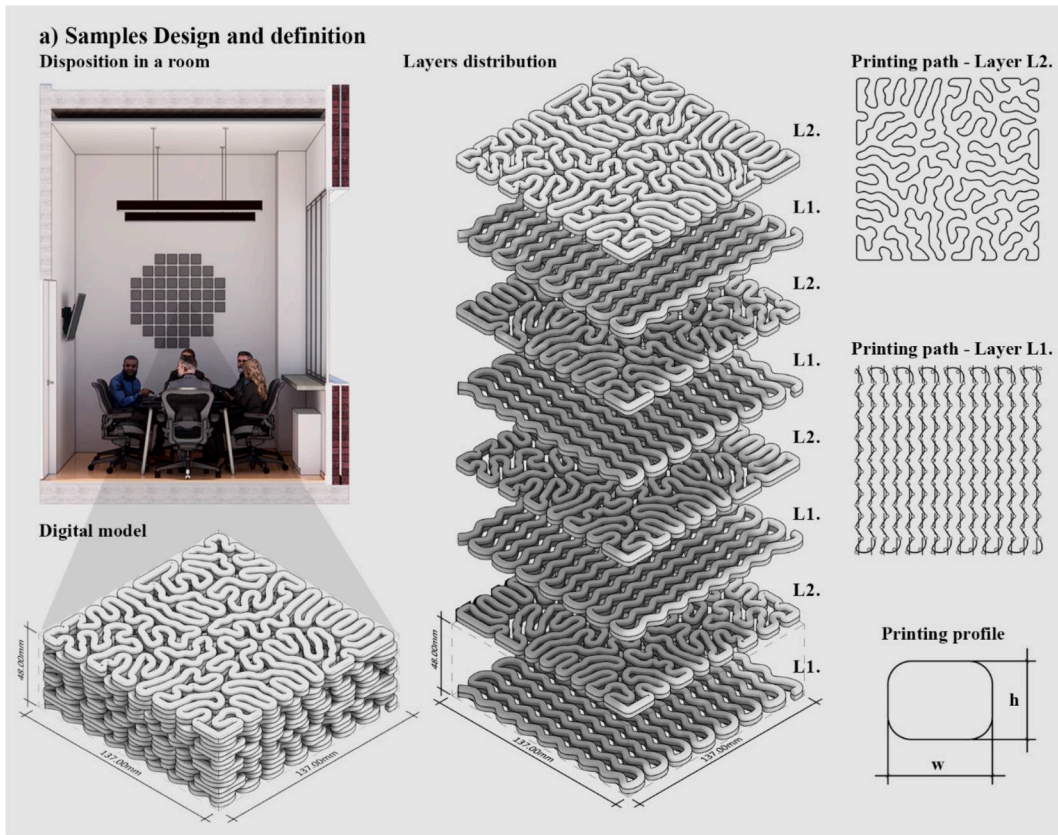
The geometrical structure was then manufactured with LDM 3D printing, always using the same original clay with some variations on its composition and treatments to investigate the impact on functional properties (especially moisture buffering).

Testing produced samples under controlled temperature and humidity conditions determined moisture buffering capabilities and influences generated by material composition, material micro/nanostructure, and the component macro-structure.

2.1. Samples and materials definition

2.1.1. Main strategy for maximizing surface area

Sample geometry maximizes the macroscopic surface area exposed to indoor air by having macrostructures that work as a 3D scaffold with interconnected open pores, enabling internal air circulation. Based on a visual algorithm implemented in Grasshopper, a parametric iteration allowed for modifications of the geometrical features while maximizing macroscopic surface area ( $S_a$  as defined in equation (1)). The sample geometry results from overlapping two layers with different printing path typologies (L1 and L2), as shown in Fig. 1a). The rationale behind this design is to have morphologies with increased surface area and to minimize printing time, using a single uninterrupted printing path both on the  $xy$  plane and  $z$  direction. Typology (L1) generates linear voids, allowing air circulation along  $x$  and  $z$  or  $y$  and  $z$  depending on the layer orientation. Typology (L2) results from an algorithm implementing a differential growth simulation of a curve inside the domain, using Kangaroo and Anemone plugins for Grasshopper (supplementary information



b) Manufactured Samples

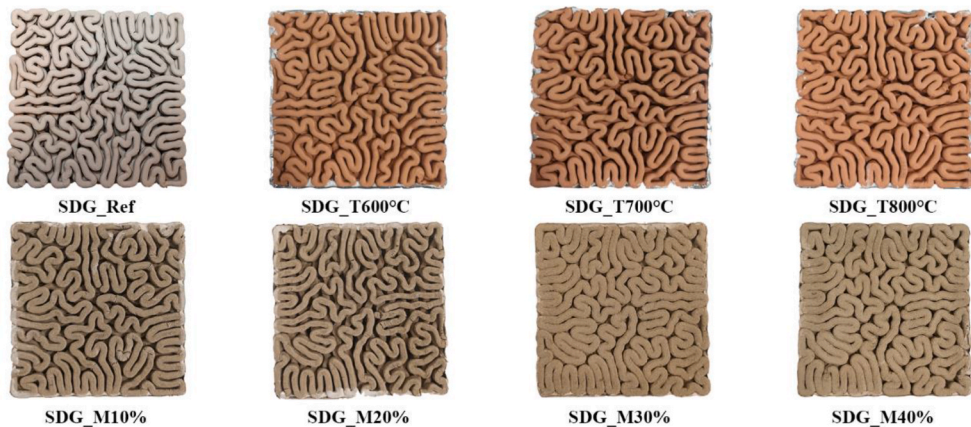


Fig. 1. Samples design definition and disposition within a room.

S2).

Final 3D geometry results from alternating the two printing paths along the z direction, particularly using a layer pattern L1-L1-L2-L2. As shown in Fig. 1a, the final component results from overlapping 16 layers, each 3 mm thick, with a total height of 48 mm.

Equation (1) estimates  $S_{a,digital}$  considering the total length of the printing path ( $L_{path}$  equal to 32.25 m for all the 16 layers), the perimeter of the printing profile perimeter ( $P_{profile}$  approximated by the rectangular shape 4 by 3 mm), and the contact zones generated by the layer overlapping areas ( $I_{area}$ ). The last reduces the available surface directly exposed to air, hence not allowing moisture transfer with the gas side.

$$S_{a,digital} = (L_{path} * P_{profile}) - I_{area} \quad (1)$$

### 2.1.2. 3D-LDM manufacturing

The LDM 3D printer Delta WASP 40100 manufacturing instructions, enclosed in the G-code of the 3D mesh, were generated directly from the Grasshopper algorithm [31,56]. This workflow replaces the slicing procedure, avoiding the additional step in a separate software while enabling a seamless transition from digital modeling to the manufacturing process. This described approach has the advantage of increasing geometrical accuracy.

The manufacturing constraints were the printing path, the nozzle diameter (4 mm), the printing speed (1800 mm/min), the printing flux (18 %), and the gross printing volume ( $137 \times 137 \times 48$  mm [3]). However, the sample drying process determines a significant shrinkage. Hence, final gross dimensions differ from post-printing, as well as from the digital.

After measuring the shrinkage on the xy plane and along z (as reported in Table 2 for each sample), the surface area after manufacturing was re-calculated considering the total shrinkage factor ( $Sf_{x,y,z}$ ) as shown in equation (2).

$$S_{a,manufacturing} = [(L_{path} * P_{profile}) * (Sf_{x,y,z})] - I_{area} \quad (2)$$

### 2.1.3. Main strategy related to clay stabilization

Due to the post-processing requirement to achieve shape stability and long-term integrity, this study undertakes a comparative analysis of two distinct treatments, focusing on comparing the effect of hygroscopic properties. In particular, evaluating moisture buffering and equilibrium moisture uptakes against material morphology and composition modifications. The comprehensive evaluation encompasses X-ray diffraction, Scanning Electron Microscopy (SEM), and energy-dispersive X-ray spectroscopy. The first analysis explores the influence of thermal treatment when firing clay-printed components at 600, 700, and 800 °C. In view of practical application, this approach is justified by the known effects of thermal treatments on the mechanical properties of clay-based products e.g., increase of elastic modulus [59,60] and flexural strength [61,62], also allowing long-term integrity upon contact with water due to the loss of hydroplastic behavior.

The second analysis assesses the influence of incorporating a mineral binder, specifically calcium hydroxide paste,  $Ca(OH)_2$ , at varying mass percentages within 10–40 %. Previous works already proposed the latter approach concerning different applications of clay-based materials for building [51]. Furthermore, it is known that adding calcium hydroxide to clay increases the material resistance to deformation under loading [63], which is also beneficial in view of practical applications of 3D-printed components.

## 2.2. Testing

### 2.2.1. Moisture Buffer Value (MBV) measurement

The practical Moisture Buffer Value ( $MBV_{practical}$ ) is a key performance indicator, representing the amount of moisture transported in or out of a material per frontal exposed area over a specific period and in response to variations in the relative humidity of surrounding air. The  $MBV_{practical}$  was evaluated according to the NORDTEST protocol [4] using a climatic chamber ATT DM340 for temperature and humidity control. Anyscales THB-3000  $\pm$  0.05 g scale measured mass variations at the beginning and the end of each step of the humidity cycle.

Before starting the MBV test, samples were preconditioned at 50 % RH and 23 °C until their mass stabilized (equilibrium achieved in 72 h, with a 0.001 % mass variation according to ISO 12571:2021). After preconditioning, the samples were exposed to 5 humidity cycles of 24 h at a constant temperature of 23 °C. Each cycle consisted of 8 h at 75 % RH, followed by 16 h at 33 %. Fig. 2 and Table 1 display the effective environmental conditions during preconditioning and the moisture buffer test cycles.

**Table 1**

MBV test conditions. Average temperature  $T_{avg}$ , relative humidity during each phase of the test  $RH_{avg}$ , and variation during sorption ( $\Delta RH_{abs}$ ) and desorption ( $\Delta RH_{des}$ ).

Interval	Cycle	$RH_{avg}$ [%]	$T_{avg}$ [°C]	$\Delta RH_{des}$ [%]	$\Delta RH_{abs}$ [%]
Absorption	C <sub>1</sub>	72.38	22.64	42.70	–
Desorption		29.67	23.58	–	41.38
Absorption	C <sub>2</sub>	71.05	22.88	40.26	–
Desorption		30.79	24.05	–	43.86
Absorption	C <sub>3</sub>	74.65	23.32	41.06	–
Desorption		33.59	23.67	–	40.61
Absorption	C <sub>4</sub>	74.20	23.48	39.40	–
Desorption		34.80	23.25	–	40.25
Absorption	C <sub>5</sub>	75.05	23.27	42.20	–
Desorption		32.85	23.55	–	–

**Table 2**  
Macroscopic data of 3D printed dry samples.

Sample Name	Material	Size [cm]	Shrinkage [%]		Wall [mm]	Mass <sub>dry</sub> [g]	S <sub>exposed</sub> [cm <sup>2</sup> ]	A <sub>specific</sub> [cm <sup>2</sup> /g]	ρ <sub>apparent</sub> [g/cm <sup>3</sup> ]
			xy	z					
<b>B0</b>	Unfired Clay	14.0 × 14.0 x 4.0	–	–	–	1398	381	0.27	1.88
<b>SDG_Ref</b>	Unfired Clay	12.7 × 12.7 x 4.5	14.1	6.3	5.3	911	3702	4.06	1.26
<b>SDG_T600°C</b>	Fired Clay	12.7 × 12.7 x 4.5	14.1	8.3	5.4	892	3715	4.16	1.26
<b>SDG_T700°C</b>		12.7 × 12.7 x 4.5	14.1	8.3	5.3	850	3715	4.36	1.20
<b>SDG_T800°C</b>		12.7 × 12.7 x 4.5	14.1	8.3	5.5	825	3702	4.52	1.16
<b>SDG_M10 %<sub>1</sub></b>	Unfired Clay with Ca(OH) <sub>2</sub> 10–40 % wt	12.3 × 12.3 x 4.3	19.4	10.4	5.3	682	3728	5.06	1.05
<b>SDG_M10 %<sub>2</sub></b>		12.3 × 12.3 x 4.3	19.4	10.4	5.6	712	3451	4.89	1.09
<b>SDG_M20 %<sub>1</sub></b>		12.4 × 12.4 x 4.3	18.1	10.4	4.7	581	3481	5.91	0.88
<b>SDG_M20 %<sub>2</sub></b>		12.4 × 12.4 x 4.3	18.1	10.4	4.9	614	3430	5.64	0.93
<b>SDG_M30 %<sub>1</sub></b>		12.2 × 12.2 x 4.3	20.7	10.4	5.6	704	3461	4.86	1.10
<b>SDG_M30 %<sub>2</sub></b>		12.2 × 12.2 x 4.3	20.7	10.4	5.8	693	3418	4.96	1.08
<b>SDG_M40 %<sub>1</sub></b>		12.1 × 12.1 x 4.3	22.0	10.4	5.8	697	3434	4.83	1.11
<b>SDG_M40 %<sub>2</sub></b>		12.1 × 12.1 x 4.3	22.0	10.4	6.1	703	3369	4.82	1.12

Furthermore, the MBV measurements involved thirteen samples, where one served as a control reference to evaluate MBV variations. The control reference (B0) had a regular full box geometry, while residual twelve were 3D printed and had the same digital geometry we called SDG (Fig. 1a).

### 2.2.2. Equilibrium moisture uptake

The moisture sorption isotherms were determined with a climatic chamber ATT DM340 at 33 %, 53 %, 73 %, 83 %, and 90 % RH, with a temperature of 23 °C, in both adsorption and desorption mode to evaluate the presence of hysteresis.

The samples were kept in the climatic chamber and weighed every 24 h until reaching the equilibrium condition at each RH step. Equation (3) shows the definition of equilibrium moisture content ( $u$ ).

$$u = \frac{m_{eq} - m_{dry}}{m_{dry}} \quad (3)$$

Where  $m_{eq}$  is the equilibrium mass of the sample at a certain RH and  $m_{dry}$  is the mass of the dry sample (ISO12570:2018).

According to ISO 12571:2021 standard, the equilibrium criteria  $u < 0,001$  % after 3 consecutive days was used, while the dry mass value results from drying samples at 105 °C in a ventilated oven for at least 20 h.

### 2.2.3. Composition, microstructure and morphology

The composition of the starting clay used in this work was assessed by energy dispersive spectroscopy (EDS); the probe was

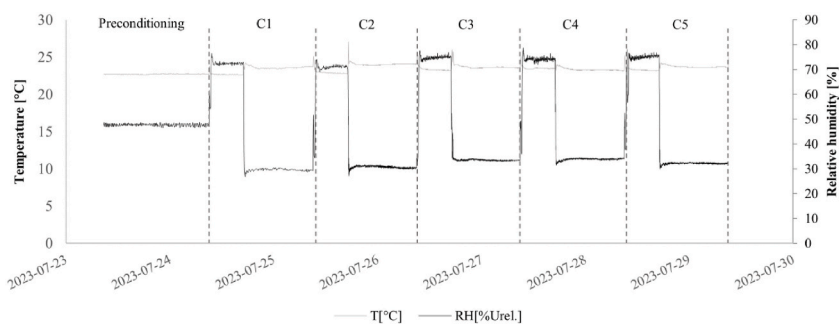


**Fig. 2.** Temperature and relative humidity conditions during the MBV test with the climatic chamber ATT DM340.

incorporated in the scanning electron microscopy (SEM) equipment (see below).

X-ray diffraction (XRD) using an equipment with Bragg-Brentano camera geometry and Cu K $\alpha$  incident radiation (wavelength of 0.15405 nm) (Malvern PANalytical X'Pert PRO diffractometer) was performed on the samples to investigate the crystalline structure. The voltage and filament current were 40 kV and 30 mA, respectively. Each sample was pulverized before the analysis. The step counting time and the step size were set at 1 s and 0.02 $^\circ$ , respectively. The 2 $\theta$  range used for such measurements was from 10 to 70 $^\circ$ . The data from the obtained spectra were analyzed, and phase identification was carried out by using the X-Pert HighScore Software with PCPDF database.

Morphological characteristics of as-such and thermally- or chemically-treated materials were investigated by SEM (JCM 6000Plus Versatile Benchtop SEM, JEOL) under an accelerating voltage of 5 kV. Samples were sputter-coated with a thin layer of chromium (less than 10 nm) before being inspected by SEM.

To further investigate the thermal influence on the clay sample's nanoporous structure, N $_2$  adsorption/desorption isotherms were measured at -196  $^\circ$ C (Quantachrome Autosorb 1C). SDG samples were previously outgassed at 100  $^\circ$ C to remove water and other atmospheric contaminants. From N $_2$  isotherms, specific surface area (SSA $_{BET}$ ) was measured by Brunauer-Emmett-Teller (BET) multipoint method in the 0.05–0.20 relative pressure range; total porous volume (V $_{TOT}$ ) was measured at p/p $_0$  = 0.97, and cumulative mesopore volume curves were obtained by applying BJH method to adsorption branch. Microporous volume (V $_{MICRO}$ ) was calculated by De Boer t-plot analysis.

### 3. Results and discussion

The utilization of additive manufacturing presents an opportunity to optimize mass utilization per unit volume. For instance, comparing the control full-volume reference configuration (B0) with the 3D-printed counterparts (SDG), which have similar overall volumes (784 cm $^3$  vs. 704 cm $^3$ ), a reduced mass of the dry component was achieved: approximately 35 % for the SDG-reference (unfired clay), about 39 % for the SDG\_T (thermal treatment), and roughly 51 % for the SDG\_M (chemical treatment).

The reduction in mass achieved through the designed SDG 3D printing pathway is closely linked to the increased macroscopic surface area directly exposed to air, which ranges from 0.27 cm $^2$ /g (reference configuration B0) to 4–6 cm $^2$ /g in the various SDG configurations. Additional mass reduction for the SDG\_T is attributed to increased water loss at higher firing temperatures. Conversely, for the SDG\_M, the introduction of Ca(OH) $_2$  significantly altered clay composition, resulting in lighter printed components due to the reduced bulk density of the paste.

Despite the set configuration of the 3D printer was consistent, the wall thickness of the final samples exhibited different values. In cases where the SDG configurations necessitated no alteration to the clay composition (unfired clay and thermal treatment), the printed wall thickness remained relatively uniform (average value of 5.3  $\pm$  0.1 mm). Samples based on SDG\_M configuration, which required the addition of CaOH $_2$  and water, had an average wall thickness of 5.5 mm, with a higher deviation equal to  $\pm$ 0.5 mm (measurements in supplementary information S1).

Each of the SDG configurations required a total printing path of 32.25 m. This extensive path accounts for a total potential printed surface of 0.41 m $^2$  per component,  $\sim$ 21 times greater than the control reference sample B0 surface of 0.02 m $^2$ . However, the surface in contact between each printing layer of clay limits the effective exposure to air. Considering this surface limitation, the SDG configurations exhibit a surface of 0.33–0.37 m $^2$ .

#### 3.1. MBV results

Fig. 3a reports the results of the MBV $_{practical}$  for each of the tested samples. The reference full and solid volume (B0) of unfired clay has an MBV of 3.27 g/(m $^2$  %RH). Thanks to a surface 21 times higher, the MBV of the printed SDG configuration, using the same clay of B0 without any treatment, achieved 10.38 g/(m $^2$  %RH), representing the highest value experienced in this study.

As expected, both the implemented strategies to increase the long-term stability of clay negatively impacted buffering performances.

The thermal treatment significantly reduces the Moisture Buffer Value (MBV), and the extent of reduction follows the trend of the temperature increase during the applied thermal treatment. Specifically, the MBV decreased sharply to 5.93 to 2.43 g/(m $^2$  %RH) as the temperature varied from 600  $^\circ$ C to 800  $^\circ$ C. This reduction in MBV, as indicated in Fig. 3a, leads to a final value even lower than the

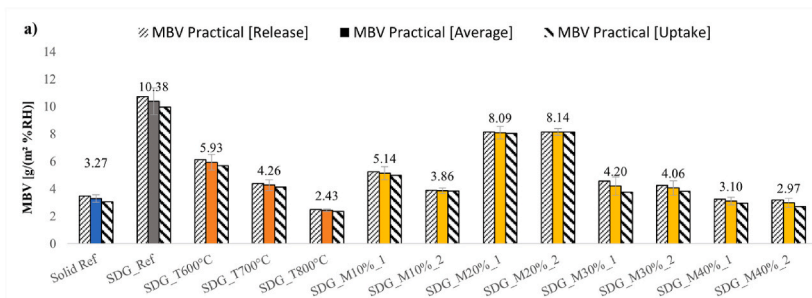


Fig. 3. Results of practical MBV measurements through the NORDTEST protocol on different produced samples.

unfired control reference B0  $3.27 \text{ g}/(\text{m}^2 \%RH)$ . This behavior is associated with the dehydroxylation of clay at elevated temperatures [64]. The heat treatment effectively minimizes the quantity of bound water within the crystalline microstructure of the clay, consequently reducing the overall dry mass of the material. Furthermore, the thermal process prompts microstructural changes, also diminishing internal porosity (see BET analysis in section 3.3.1) and decreasing moisture transportation capabilities. These changes adversely impact macroscopic performances assessed through the MBV evaluation, producing a less porous material with lower moisture-absorbing capacity (section 3.2) because of the decomposition of layered structure in clay minerals.

As regards the mixes with  $\text{Ca}(\text{OH})_2$ , the viscosity of the material influences printability, which requires manual adjustments of water content between 6 and 10 % to allow good printing quality. This process was not systematically explored, generating a disturbance in the  $\text{Ca}(\text{OH})_2$  trend of Fig. 3, and will be the topic of further studies.

### 3.2. Equilibrium moisture uptake

Fig. 4 shows the influence of the stabilization methods, thermal versus chemical treatment, in terms of adsorption capacity variation on different samples. Supplementary information S3 reports the exact values of the isotherms with the monitored temperature and relative humidity within the climatic chamber. To comply with the equilibrium constraints defined in ISO 12571:2021 over the different RH steps, a testing period of two months was necessary.

Fig. 4a, in particular, depicts the significant reduction of adsorption capacity associated with clay firing temperature (600 °C, 700 °C, and 800 °C) when compared with reference clay (just dried at 105 °C). In all cases, a hysteresis loop is well evident, resulting in higher moisture uptake during the desorption stage than the adsorption values. The increased firing temperature does not affect the hysteresis, except for humidity higher than 80 %, reducing the difference between the moisture capacity in adsorption and desorption.

On the contrary, Fig. 4b shows that the inclusion of  $\text{Ca}(\text{OH})_2$  has a much less prominent effect on reducing moisture adsorption capacity, resulting in an overlap of all different adsorption and desorption curves. The hysteresis area reduces as the  $\text{Ca}(\text{OH})_2$  content increases, thus reducing the differences between adsorption and desorption values.

This trend, together with the MBV analysis and the morphological assessments, indicates that using  $\text{Ca}(\text{OH})_2$  leaves a material with characteristics much more similar to unfired clay, preserving hygroscopic performances while stabilizing the internal structure.

### 3.3. Materials morphology and microstructures

#### 3.3.1. Effect of thermal treatment

The assessment of oxide composition (wt.%) by EDS revealed the presence of  $\text{SiO}_2$  (31.3 %),  $\text{CaO}$  (31.0 %),  $\text{F}_2\text{O}_3$  (17.6 %),  $\text{Al}_2\text{O}_3$  (13.3 %),  $\text{MgO}$  (2.4 %),  $\text{Na}_2\text{O}$  (0.3 %) and C (4.1 %).

Fig. 5 presents the morphological analysis of the clay using SEM. SEM photographs exhibit microstructural changes between dried and fired clay at different temperatures.

Dried clay at 105 °C (Fig. 5a and b) is characterized by lamellar and small-plate crystals. The structure remains similar when the clay is treated at 600 °C (Fig. 5c and d). These microstructures, composed of thin and lamellar plates, are associated with the presence of kaolinite and montmorillonite [65]. The microstructure remains essentially the same up to 900 °C: the typical platy-like crystals are well visible, and the surfaces exhibit a significant roughness as sintering has not started yet.

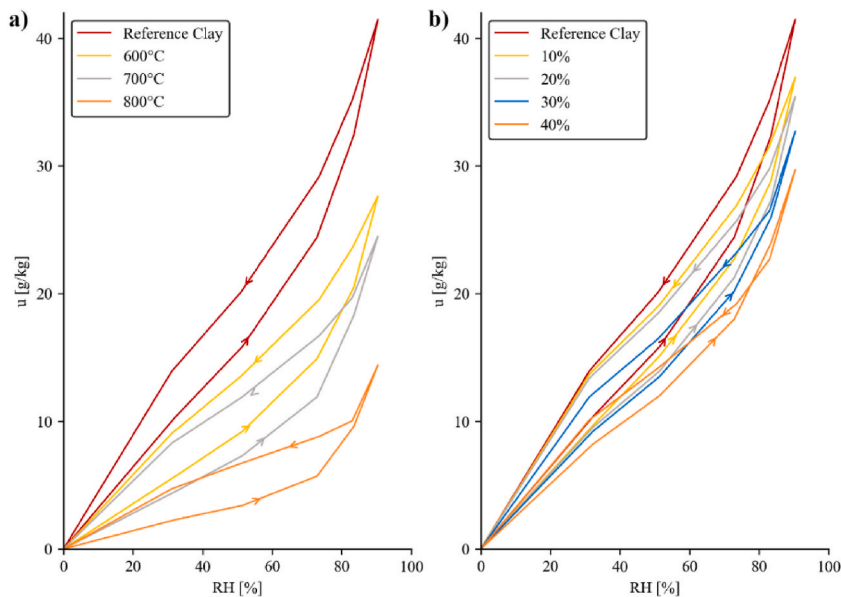
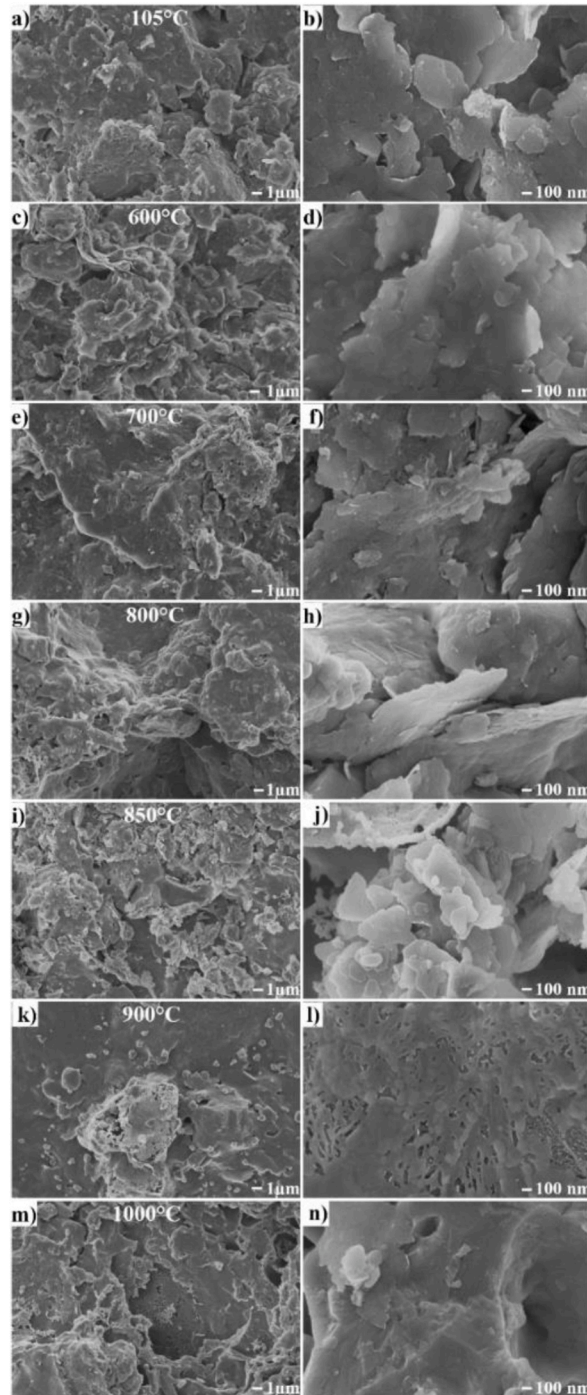


Fig. 4. Sorption/Desorption isotherms: a) the influence on adsorption and desorption isotherm and related hysteresis after clay stabilization with a thermal treatment at 600, 700, and 800 °C; b) the influence on adsorption and desorption isotherm and related hysteresis when clay composition is modified using 10 %, 20 %, 30 % and 40 % of  $\text{Ca}(\text{OH})_2$  in mass.



**Fig. 5.** Different SEM images show morphological modifications of the samples when the firing temperature varies from 600 to 1000 °C. In particular, pictures on the left a), c), e), g), i), k), and m) show the sample morphology with a magnification of 10,000× when the temperature is respectively 105 °C, 600 °C, 700 °C, 800 °C, 850 °C, 900 °C, and 1000 °C, while the pictures on the right, b), d), f), h), j), l), and n), show the influence of the same thermal treatments but with a magnification of 100,000×.

The sintering process begins to be observed at 900 °C (Fig. 5k and l), and densification becomes more evident as the treatment temperature increases. Fig. 5l shows the presence of sintering necks, yielding an evident densification of clay particles, and at 1000 °C, a smoother surface with much less roughness can be seen (Fig. 5m).

Fig. 6 reports the XRD patterns obtained from the analysis of dried and sintered clay undergoing thermal treatments at different temperatures.

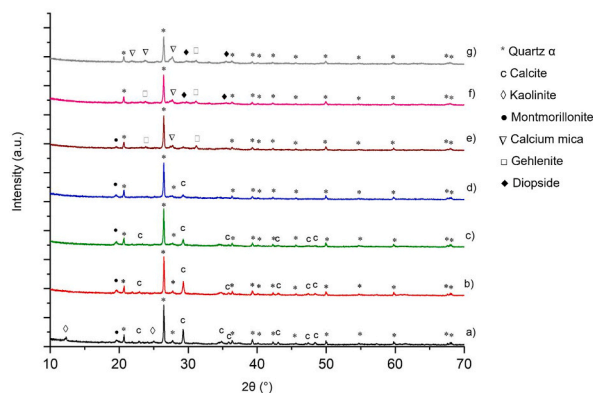


Fig. 6. Results of XRD measurements for samples stabilized with a thermal treatment. XRD pattern of a) dried clay and clay treated at b) 600 °C, c) 700 °C, d) 800 °C, e) 850 °C, f) 900 °C, g) 1000 °C.

The dried and fired clay XRD patterns show Quartz  $\alpha$  as a major component. Quartz  $\alpha$  has a trigonal structure, which is stable at room temperature until 573 °C. When the temperature increase leads to an  $\alpha \rightarrow \beta$  quartz inversion at around 600 °C, the structure changes in hexagonal, but when the quartz  $\beta$  is cooled below 573 °C it transforms rapidly again to quartz  $\alpha$  [65].

Other crystalline phases detected in the starting material are calcite ( $\text{CaCO}_3$ ), kaolinite ( $\text{Na}_{0.3}\text{Al}_4\text{Si}_6\text{O}_{15}(\text{OH})_6 \cdot 4\text{H}_2\text{O}$ ), and montmorillonite ( $(\text{Na},\text{Ca})_{0.3}(\text{Al},\text{Mg})_2\text{Si}_4\text{O}_{16}(\text{OH})_2 \cdot x\text{H}_2\text{O}$ ). A summary of crystalline phases is reported in Table 3.

The intensities of the peaks related to the calcite phase progressively decrease as the temperature increases; at 800 °C (Fig. 6d), only one peak at  $2\theta = 29.3^\circ$  was detected for calcite with a significantly lower intensity compared to the samples treated at lower temperatures. This happens because of the decarbonation of calcite upon temperature increase, starting from 650 °C up to 850 °C [59].

However, phase decomposition and phase transformation reactions occur during thermal treatments, leading to kaolinite dehydroxylation [66] once the temperature is higher than 500 °C and disappearing from the XRD patterns at higher temperatures.

According to the XRD patterns reported in curves b), c), d), and e) of Fig. 6, the characteristic peak associated with montmorillonite at  $2\theta = 19.72^\circ$  [67] progressively decreases in intensity as the heating temperature increases above 700 °C [68].

At the firing temperature of 850 °C (Fig. 6e), Quartz  $\alpha$  remains the predominant phase, but Calcium mica ( $\text{Al}_3\text{Ca}_{0.5}\text{Si}_3\text{O}_{11}$ ) and Gehlenite ( $\text{Ca}_2\text{Al}_2\text{SiO}_7$ ) appear as well. Gehlenite is a metastable phase, and the degree of its crystallinity increases within the temperature range of 900–1000 °C while it reduces at higher temperatures [69,70].

The formation of gehlenite begins with the thermal decomposition of calcite and kaolinite, leading to the generation of lime and metakaolinite. These reactive phases subsequently react to form gehlenite [71]. At 900 °C and 1000 °C, the formation of Diopside ( $\text{CaMgSi}_2\text{O}_6$ ) starts as well. This mineral is a common metastable high-firing phase whose presence is related to the composition of the raw clay.

Diopside appears after a reaction between three oxides: CaO originated from calcite, MgO from montmorillonite, and  $\text{SiO}_2$  from kaolinite in the clay [72]. Diopside is typically identified from 900 °C and is more abundant at 1000 °C [70,73], consistent with our experimental findings.

The effect of the thermal treatment on the porous properties of the SDG clay was further investigated by means of  $\text{N}_2$  adsorption measurements at 77 K, the results of which are gathered in Fig. 7 and Table 4. The samples treated at  $T \leq 800$  °C show Type II isotherms with narrow H3 hysteresis loop, the latter disappearing for  $T = 1000$  °C. The loop shows a lower limit of the desorption branch located at the cavitation-induced  $p/p_0$  (ca. 0.4), as typically observed for agglomerates of plate-like particles containing slit-shaped pores [74]. Furthermore, the  $\text{N}_2$  isotherms of the samples do not show any evident steep initial portion at low relative pressure, indicating a limited microporosity of the samples. Actually, some intra-particle microporosity (i.e. pore width  $< 2$  nm) may be expected due to the presence of montmorillonite, but the interlayer spacing of montmorillonites exchanged with small metal cations (such as  $\text{Na}^+$ ,  $\text{Ca}^{2+}$  and  $\text{K}^+$ ) is usually too small to be fully accessible to  $\text{N}_2$  at 77 K [75]. Therefore, the measured  $\text{SSA}_{\text{BET}}$  values are predominantly due to particles external surface and mesoporosity. In the case of clays, mesopores (2–50 nm in diameter) are mainly due to interparticle pores

Table 3

Name, chemical formula, and reference code (from ICDD PDF database) of the phases identified in XRD measurements.

Compound Name	Chemical Formula	Reference Code
Quartz $\alpha$	$\text{SiO}_2$	01-085-0462
Kaolinite	$\text{Na}_{0.3}\text{Al}_4\text{Si}_6\text{O}_{15}(\text{OH})_6 \cdot 4\text{H}_2\text{O}$	00-029-1490
Montmorillonite	$(\text{Na},\text{Ca})_{0.3}(\text{Al},\text{Mg})_2\text{Si}_4\text{O}_{16}(\text{OH})_2 \cdot x\text{H}_2\text{O}$	00-012-0232
Calcium Mica	$\text{Al}_3\text{Ca}_{0.5}\text{Si}_3\text{O}_{11}$	00-046-0744
Gehlenite	$\text{Ca}_2\text{Al}_2\text{SiO}_7$	01-089-5917
Diopside	$\text{CaMgSi}_2\text{O}_6$	01-075-1092
Calcite	$\text{CaCO}_3$	01-086-2334
Calcium Hydroxide	$\text{Ca}(\text{OH})_2$	01-084-1265

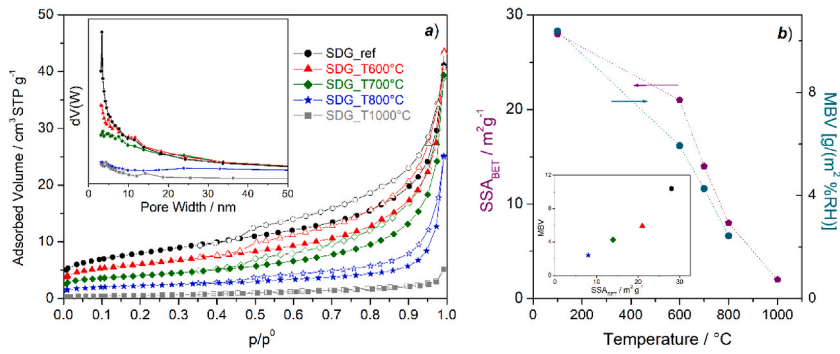


Fig. 7. Analysis of porosity: (a): N<sub>2</sub> adsorption/desorption isotherms at 77 K of dried clay (black circles) and clay treated at 600 °C (red triangles), 700 °C (green diamonds), 800 °C (blue stars) and 1000 °C (gray squares); BJH mesopore size distribution (inset). (b) correlation of SSA<sub>BET</sub> and MBV with temperature of the thermal treatment. (For interpretation of the references to colour in this figure legend, the reader is referred to the Web version of this article.)

Table 4

Porous properties as obtained from N<sub>2</sub> isotherms at 77 K.

Sample	SSA <sub>BET</sub> /m <sup>2</sup> g <sup>-1</sup>	V <sub>TOT</sub> /cm <sup>3</sup> g <sup>-1</sup>	V <sub>MICRO</sub> <sup>a</sup> /cm <sup>3</sup> g <sup>-1</sup>
SDG_ref	28	5·10 <sup>-2</sup>	3·10 <sup>-3</sup>
SDG_600 °C	21	4·10 <sup>-2</sup>	3·10 <sup>-3</sup>
SDG_700 °C	14	4·10 <sup>-2</sup>	2·10 <sup>-3</sup>
SDG_800 °C	8	2·10 <sup>-2</sup>	1·10 <sup>-3</sup>
SDG_1000 °C	2	5·10 <sup>-3</sup>	0

<sup>a</sup> As calculated by De Boer t-plot analysis.

produced by the microstructural arrangement of the clay mineral particles [76].

### 3.3.2. Effect of mixing with Ca(OH)<sub>2</sub>

Fig. 8 shows the morphological influence of Ca(OH)<sub>2</sub> on clay microstructure. The presence of Ca(OH)<sub>2</sub> is associated with observing additional extremely fine particles, which are absent in the image of the as-such dried clay (Fig. 5a). The lamellar microstructures of clay are preserved regardless of the amount of Ca(OH)<sub>2</sub>; kaolinite and montmorillonite still exist, as confirmed by the XRD analysis (Fig. 9). There are no significant variations among the XRD patterns, and in particular, the peaks associated with the presence of kaolinite and montmorillonite are still present. In addition, as expected, new peaks were associated with the presence of Ca(OH)<sub>2</sub> in the mixes (see Table 3) where calcium hydroxide was added in an amount equal to or above 20 wt% (Fig. 9d–e). The peaks associated with this phase increase as the amount in the mix increases.

The XRD and SEM analysis demonstrated that the clay morphology when adding Ca(OH)<sub>2</sub> does not change too much if compared with dry clay. Indeed, as shown in Fig. 9, adding the calcium hydroxide preserves the presence of two important elements, kaolinite and montmorillonite. These two crystalline phases are important for the hygroscopic properties of moisture uptake to the clay [77]. Differently, high-temperature thermal treatment leads to deep degradation of these two structures (especially kaolinite) as well as decrement of porosity, yielding degradation of moisture uptake capability.

## 4. Conclusions

This study investigated the potential of 3D-printed clay components as a sustainable solution for passive indoor moisture buffering. By comparing innovative 3D designs with traditional full-volume unfired clay blocks, we examined the influence of stabilization procedures on hygroscopic properties, moisture buffering capacity, porosity, and morphology.

Additive manufacturing using LDM technology significantly increased the practical MBV of different components, elevating the macroscopic surface area exposed to the indoor air from 3.27 to 10.38 g/(m<sup>2</sup> %RH), as the macroscopic surface area increased from 0.27 to 4.06 cm<sup>2</sup>/g. Achieved MBV values are classified as excellent or more, according to the NORDTEST protocol.

Various thermal treatments of 3D-printed components resulted in decreased equilibrium moisture uptake and reduced MBV, reaching 5.93 and 2.43 g/(m<sup>2</sup> %RH), respectively at 600 °C and 800 °C. In this regard, nitrogen adsorption-desorption measurements confirmed a decrease in the material nanoporosity, consistently with the functional assessment (MBV decrement with firing temperature). Alternatively, incorporating Ca(OH)<sub>2</sub> into the clay composition led to less degradation of equilibrium moisture uptake and buffering performance compared to thermal treatment. XRD and SEM analyses showed that adding Ca(OH)<sub>2</sub> did not significantly alter the clay morphology compared to unfired clay. Unlike thermal treatment, adding calcium hydroxide within 40 % preserved the presence of clay components for water affinity, kaolinite, and montmorillonite. Conversely, high-temperature thermal treatment led to significant degradation of these structures, particularly kaolinite. The results achieved in this paper motivate further investigations following the approaches proposed addressed to final use in a real building scenario.

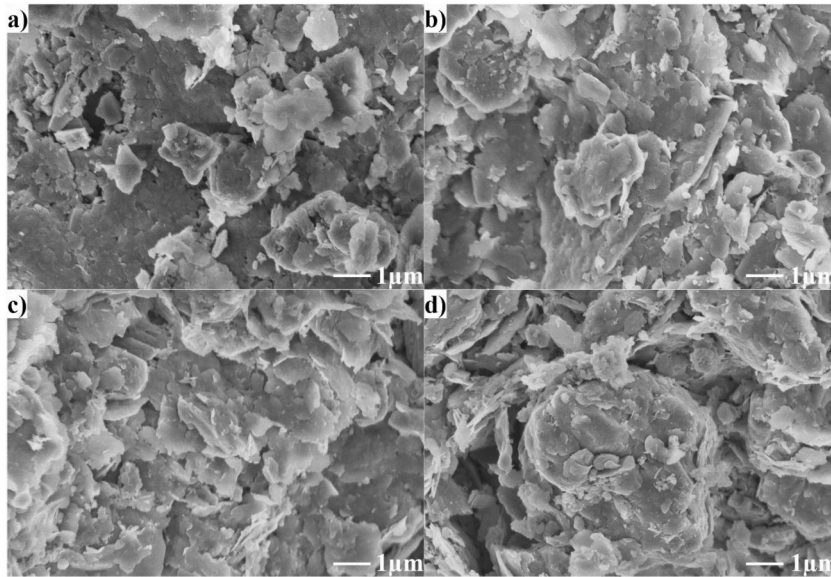


Fig. 8. Different SEM images show morphological modifications of clay when different amounts of  $\text{Ca(OH)}_2$  have been added to the mixture. From a) to d), the mass content of  $\text{Ca(OH)}_2$  is 10 wt%, 20 wt%, 30 wt%, and 40 wt%. All magnifications in the images are 10,000 $\times$ .

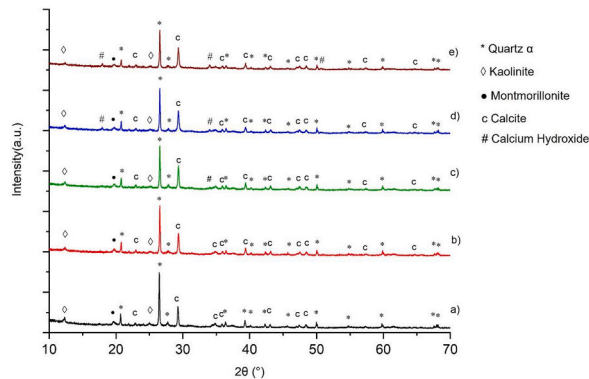


Fig. 9. Results of XRD measurements for samples stabilized with  $\text{Ca(OH)}_2$ . XRD pattern of a) dried clay and clay with  $\text{Ca(OH)}_2$  with mass percentages of b) 10 %, c) 20 %, d) 30 %, e) 40 %.

**CRedit authorship contribution statement**

**Vincenzo Gentile:** Writing – review & editing, Writing – original draft, Validation, Supervision, Methodology, Investigation, Data curation, Conceptualization. **Juan Diego Vargas Velasquez:** Writing – review & editing, Writing – original draft, Visualization, Investigation, Data curation, Conceptualization. **Stefano Fantucci:** Writing – review & editing, Supervision, Methodology, Funding acquisition, Conceptualization. **Giorgia Autretto:** Writing – review & editing, Investigation. **Roberta Gabrieli:** Writing – review & editing, Writing – original draft, Visualization, Investigation, Data curation. **Pardeep Kumar Gianchandani:** Writing – review & editing, Investigation. **Marco Armandi:** Writing – review & editing, Investigation, Data curation. **Francesco Baino:** Writing – review & editing, Supervision, Methodology, Funding acquisition, Conceptualization.

**Declaration of competing interest**

The authors declare that they have no known competing financial interests or personal relationships that could have appeared to influence the work reported in this paper.

**Data availability**

Data will be made available on request.

## Acknowledgements

This research work was performed in the frame of a project funded under the National Recovery and Resilience Plan (NRRP), Mission 4 Component 2 Investment 1.3 - Call for tender No. 1561 of 11.10.2022 of Ministero dell'Università e della Ricerca (MUR); the project was funded by the European Union – NextGenerationEU. Project details: project code PE0000021, Concession Decree No. 1561 of 11.10.2022 adopted by Ministero dell'Università e della Ricerca (MUR), CUP E13C22001890001, Project title “Network 4 Energy Sustainable Transition – NEST”.

The authors wish to acknowledge Eng. Pierpaolo Nuzzo who supported 3D printing process and Ms Valeria Villamil Cardenas for the support provided during the testing phase at the Department of Energy (Politecnico di Torino).

## Appendix A. Supplementary data

Supplementary data to this article can be found online at <https://doi.org/10.1016/j.jobbe.2024.109631>.

## References

- [1] K. Zu, M. Qin, C. Rode, M. Libralato, Development of a moisture buffer value model (MBM) for indoor moisture prediction, *Appl. Therm. Eng.* 171 (2020) 115096.
- [2] M. Zhang, M. Qin, C. Rode, Z. Chen, Moisture buffering phenomenon and its impact on building energy consumption, *Appl. Therm. Eng.* 124 (2017) 337–345.
- [3] N.M.M. Ramos, J.M.P.Q. Delgado, V.P. De Freitas, Influence of finishing coatings on hygroscopic moisture buffering in building elements, *Construct. Build. Mater.* 24 (2010) 2590–2597.
- [4] C. Rode, et al., *Moisture Buffering of Building Materials*, Technical University of Denmark, Department of Civil Engineering, 2005.
- [5] S. Liuzzi, M.R. Hall, P. Stefanizzi, S.P. Casey, Hygrothermal behaviour and relative humidity buffering of unfired and hydrated lime-stabilised clay composites in a Mediterranean climate, *Build. Environ.* 61 (2013) 82–92.
- [6] S. Cerolini, M. D'Orazio, C. Di Perna, A. Stazi, Moisture buffering capacity of highly absorbing materials, *Energy Build.* 41 (2009) 164–168.
- [7] Z. Pavlík, et al., Modified lime-cement plasters with enhanced thermal and hygric storage capacity for moderation of interior climate, *Energy Build.* 126 (2016) 113–127.
- [8] I. Palomar, G. Barluenga, J. Puentes, Lime-cement mortars for coating with improved thermal and acoustic performance, *Construct. Build. Mater.* 75 (2015) 306–314.
- [9] Y. Jiang, et al., Improvement of water resistance of hemp woody substrates through deposition of functionalized silica hydrophobic coating, while retaining excellent moisture buffering properties, *ACS Sustain. Chem. Eng.* 6 (2018) 10151–10161.
- [10] H. Affan, W. Arairo, J. Arayro, Mechanical and thermal characterization of bio-sourced mortars made from agricultural and industrial by-products, *Case Stud. Constr. Mater.* 18 (2023) e01939.
- [11] M. Charai, A. Mezhrab, L. Moga, M. Karkri, Hygrothermal, mechanical and durability assessment of vegetable concrete mixes made with Alfa fibers for structural and thermal insulating applications, *Construct. Build. Mater.* 335 (2022) 127518.
- [12] A. Ibrahim, E. Mahmoud, M. Yamin, V.C. Patibandla, Experimental study on Portland cement pervious concrete mechanical and hydrological properties, *Construct. Build. Mater.* 50 (2014) 524–529.
- [13] N. Chennouf, B. Agoudjil, A. Boudenne, K. Benzarti, F. Bouras, Hygrothermal characterization of a new bio-based construction material: concrete reinforced with date palm fibers, *Construct. Build. Mater.* 192 (2018) 348–356.
- [14] V. Cascione, D. Maskell, A. Shea, P. Walker, The moisture buffering performance of plasters when exposed to simultaneous sinusoidal temperature and RH variations, *J. Build. Eng.* 34 (2021) 101890.
- [15] A. Ranesi, P. Faria, M.D.R. Veiga, Traditional and modern plasters for built heritage: suitability and contribution for passive relative humidity regulation, *Heritage* 4 (2021) 2337–2355.
- [16] F. McGregor, A. Heath, A. Shea, M. Lawrence, The moisture buffering capacity of unfired clay masonry, *Build. Environ.* 82 (2014) 599–607.
- [17] C.J. Simonson, M. Salonvaara, T. Ojanen, The effect of structures on indoor humidity - possibility to improve comfort and perceived air quality, *Indoor Air* 12 (2002) 243–251.
- [18] K.D. Lim, D. Maskell, Development of methods to measure the potential of a plaster to regulate indoor humidity, *Build. Serv. Eng. Res. Technol.* 42 (2021) 559–566.
- [19] X. He, H. Zhang, L. Qiu, Z. Mao, C. Shi, Hygrothermal performance of temperature-humidity controlling materials with different compositions, *Energy Build.* 236 (2021) 110792.
- [20] A. Antunes, P. Faria, V. Silva, A. Brás, Rice husk-earth based composites: a novel bio-based panel for buildings refurbishment, *Construct. Build. Mater.* 221 (2019) 99–108.
- [21] D.M. Nguyen, A.C. Grillet, T.M.H. Diep, C.N. Ha Thuc, M. Woloszyn, Hygrothermal properties of bio-insulation building materials based on bamboo fibers and bio-glues, *Construct. Build. Mater.* 155 (2017) 852–866.
- [22] B. Mazhoud, F. Collet, S. Prétot, C. Lanos, Effect of hemp content and clay stabilization on hygric and thermal properties of hemp-clay composites, *Construct. Build. Mater.* 300 (2021) 123878.
- [23] V. Gentile, M. Libralato, S. Fantucci, L. Shtrepi, G. Autretto, Enhancement of the hygroscopic and acoustic properties of indoor plasters with a super adsorbent calcium alginate BioPolymer, *J. Build. Eng.* 76 (2023) 107147.
- [24] V. Gentile, M. Libralato, S. Fantucci, L. Shtrepi, G. Autretto, Enhancement of the hygroscopic and acoustic properties of indoor plasters with a super adsorbent calcium alginate BioPolymer, *J. Build. Eng.* 76 (2023) 107147.
- [25] Z. Yang, W. Zhang, X. Lin, Q. Xiong, Q. Jiang, Optimization of minor-LiCl-modified gypsum as an effective indoor moisture buffering material for sensitive and long-term humidity control, *Build. Environ.* 229 (2023) 109962.
- [26] D.M. Ruthven, *Principles of Adsorption and Adsorption Processes*, 1984.
- [27] M.J. Cunningham, Effective penetration depth and effective resistance to moisture transfer, *Build. Environ.* 27 (1992) 379–386.
- [28] T. Arends, L. Pel, D. Smeulders, Moisture penetration in oak during sinusoidal humidity fluctuations studied by NMR, *Construct. Build. Mater.* 166 (2018) 196–203.
- [29] H. Zhang, C. Shi, D. Pan, Y. Xuan, X. He, Optimization of effective moisture penetration depth model considering airflow velocity for gypsum-based materials, *J. Build. Eng.* 32 (2020) 101539.
- [30] M. Posani, et al., Re-thinking Indoor Humidity Control Strategies: the potential of additive manufacturing with low-carbon, super hygroscopic materials, *Nat. Commun.* (2023) (Submitted in November 2023) 0–17.
- [31] J. Clarke-Hicks, I. Ochoa, D. Correa, Harnessing plastic deformation in porous 3D printed ceramic light screens, *Architect. Struct. Construct.* 3 (2023) 193–204.
- [32] G. Postiglione, G. Natale, G. Griffini, M. Levi, S. Turri, Conductive 3D microstructures by direct 3D printing of polymer/carbon nanotube nanocomposites via liquid deposition modeling, *Composites Part A Appl Sci Manuf* 76 (2015) 110–114.

- [33] M. Rosenthal, C. Henneberger, A. Gutkes, C.T. Bues, Liquid Deposition Modeling: a promising approach for 3D printing of wood, *European J. Wood Prod.* 76 (2018) 797–799.
- [34] Y. Zhang, et al., Comparison of printability and mechanical properties of rigid and flexible fiber-reinforced 3D printed cement-based materials, *Construct. Build. Mater.* 400 (2023) 132750.
- [35] S. Pessoa, M. Jesus, A.S. Guimarães, S.S. Lucas, N. Simões, Experimental characterisation of hygrothermal properties of a 3D printed cementitious mortar, *Case Stud. Constr. Mater.* 19 (2023).
- [36] Z. Li, W. Xing, J. Sun, X. Feng, Multiscale structural characteristics and Heat–Moisture properties of 3D printed building Walls: a review, *Construct. Build. Mater.* 365 (2023) 130102.
- [37] Y.A. Al-Noaimat, et al., 3D printing of limestone-calcined clay cement: a review of its potential implementation in the construction industry, *Results Eng.* 18 (2023) 101115.
- [38] A. Paolini, S. Kollmannsberger, E. Rank, Additive manufacturing in construction: a review on processes, applications, and digital planning methods, *Addit. Manuf.* 30 (2019).
- [39] T.S. Rushing, et al., Investigation of concrete mixtures for additive construction. *3D Concrete Printing Technology: Construction and Building Applications*, Elsevier Inc., 2019, <https://doi.org/10.1016/B978-0-12-815481-6.00007-5>.
- [40] M. Chougan, et al., Effect of natural and calcined halloysite clay minerals as low-cost additives on the performance of 3D-printed alkali-activated materials, *Mater. Des.* 223 (2022) 111183.
- [41] P.R. de Matos, et al., Effect of the superplasticizer addition time on the fresh properties of 3D printed limestone calcined clay cement (LC3) concrete, *Case Stud. Constr. Mater.* 19 (2023).
- [42] S.S.L. Chan, R.M. Pennings, L. Edwards, G.V. Franks, 3D printing of clay for decorative architectural applications: effect of solids volume fraction on rheology and printability, *Addit. Manuf.* 35 (2020) 101335.
- [43] E.E. Anyanwu, Design and measured performance of a porous evaporative cooler for preservation of fruits and vegetables, *Energy Convers. Manag.* 45 (2004) 2187–2195.
- [44] Y.K. Abdallah, A.T. Estévez, 3D-Printed biodigital clay bricks, *Biomimetics* 6 (2021) 1–15.
- [45] M. Bruggi, A. Taliércio, Design of masonry blocks with enhanced thermomechanical performances by topology optimization, *Construct. Build. Mater.* 48 (2013) 424–433.
- [46] Y. Ji, P. Poullain, N. Leklou, The selection and design of earthen materials for 3D printing, *Construct. Build. Mater.* 404 (2023) 133114.
- [47] A. Alqenaee, A. Memari, Experimental study of 3D printable cob mixtures, *Construct. Build. Mater.* 324 (2022) 126574.
- [48] F. Anjum, A. Ghaffar, Y. Jamil, M.I. Majeed, Effect of sintering temperature on mechanical and thermophysical properties of biowaste-added fired clay bricks, *J. Mater. Cycles Waste Manag.* 21 (2019) 503–524.
- [49] M. Mouiya, et al., Effect of sintering temperature on the microstructure and mechanical behavior of porous ceramics made from clay and banana peel powder, *Results Mater.* 4 (2019).
- [50] T. Yu, et al., Optimization of mechanical performance of limestone calcined clay cement: effects of calcination temperature of nanosized tubular halloysite, gypsum content, and water/binder ratio, *Construct. Build. Mater.* 389 (2023) 131709.
- [51] L. Chen, X. Chen, H. Wang, X. Huang, Y. Song, Mechanical properties and microstructure of lime-treated red clay, *KSCE J. Civ. Eng.* 25 (2021) 70–77.
- [52] R. Darange, A. Adesina, S. Das, Feasibility study on the sustainable utilization of uncalcined clay soils as Low-Cost binders, *Construct. Build. Mater.* 340 (2022) 127724.
- [53] T. Ahlfeld, G. Cidonio, D. Kilian, S. Duin, A.R. Akkineni, J.I. Dawson, S. Yang, A. Lode, R.O.C. Oreffo, M. G. Development of a clay based bioink for 3D cell printing for skeletal application, *Biofabrication* 9 (2017) 034103.
- [54] I. Díaz-Herrezuelo, L. Moreno-Sanabria, P. Miranzo, M.I. Osendi, M. Belmonte, Novel 3D thermal energy storage materials based on highly porous patterned printed clay supports infiltrated with molten nitrate salts, *Addit. Manuf.* 59 (2022) 103108.
- [55] Y. He, Y. Zhang, C. Zhang, H. Zhou, Energy-saving potential of 3D printed concrete building with integrated living wall, *Energy Build.* 222 (2020) 110110.
- [56] V. Sangiorgio, F. Parisi, F. Fieni, N. Parisi, The new boundaries of 3D-printed clay bricks design: printability of complex internal geometries, *Sustainability* 14 (2022).
- [57] L. Yuan, S. Ding, C. Wen, Additive manufacturing technology for porous metal implant applications and triple minimal surface structures: a review, *Bioact. Mater.* 4 (2019) 56–70.
- [58] S.S.L. Chan, R.M. Pennings, L. Edwards, G.V. Franks, 3D printing of clay for decorative architectural applications: effect of solids volume fraction on rheology and printability, *Addit. Manuf.* 35 (2020) 101335.
- [59] P.M. Nigay, T. Cutard, A. Nzihou, The impact of heat treatment on the microstructure of a clay-based ceramic and its thermal and mechanical properties, *Ceram. Int.* (2016), <https://doi.org/10.1016/j.ceramint.2016.10.084>.
- [60] T. Húlan, et al., Young's Modulus of Di Erent Illitic Clays during Heating and Cooling Stage of Firing, vols. 1–14, 2020, <https://doi.org/10.3390/ma13214968>.
- [61] V.G. Lee, T.H. Yeh, Sintering effects on the development of mechanical properties of fired clay ceramics, *Mater. Sci. Eng., A* 485 (2008) 5–13.
- [62] Y. Chalouati, A. Bennour, F. Mannai, E. Srasra, Characterization, thermal behaviour and firing properties of clay materials from Cap Bon Basin, north-east Tunisia, for ceramic applications, *Clay Miner.* 55 (2021) 351–365.
- [63] I. Goldberg, A. Klein, Some effects of treating expansive clays with calcium hydroxide. *Symposium on Exchange Phenomena in Soils*, 2009, pp. 53–71, <https://doi.org/10.1520/stp46254s>.
- [64] A.Z. Khalifa, Y. Pontikes, J. Elsen, Ö. Cizer, Comparing the reactivity of different natural clays under thermal and alkali activation, *RILEM Tech. Lett.* 4 (2019) 74–80.
- [65] M. Milošević, P. Dabić, S. Kovač, L. Kaluderović, M. Logar, Mineralogical study of clays from Dobrodo, Serbia, for use in ceramics, *Clay Miner.* 54 (2019) 369–377.
- [66] C. Sgarlata, A. Formia, C. Siligardi, F. Ferrari, C. Leonelli, Mine clay washing residues as a source for alkali-activated binders, *Materials* 15 (2022) 1–14.
- [67] B.A. Fil, C. Özmetin, M. Korkmaz, Characterization and electrokinetic properties of montmorillonite, *Bulg. Chem. Commun.* 46 (2014) 258–263.
- [68] R.E. Grim, W.F.B. Investigation, Of the Effect of Heat on the Clay Minerals Illite and Montmorillonite, vol. 23, 1939, pp. 242–248.
- [69] H. El-Didamony, K.A. Khalil, M.S. El-Attar, Physicochemical characteristics of fired clay-limestone mixes, *Cement Concr. Res.* 30 (2000) 7–11.
- [70] M. El Ouahabi, L. Daoudi, F. Hatert, N. Fagel, Modified mineral phases during clay ceramic firing, *Clay Clay Miner.* 63 (2015) 404–413.
- [71] P. Ptáček, T. Opravil, F. Soukal, J. Havlica, R. Holešinský, Kinetics and mechanism of formation of gehlenite, Al-Si spinel and anorthite from the mixture of kaolinite and calcite, *Solid State Sci.* 26 (2013) 53–58.
- [72] M.A. Harech, et al., Effect of temperature and clay addition on the thermal behavior of phosphate sludge, *Bol. Soc. Espanola Ceram. Vidr.* 60 (2021) 194–204.
- [73] I.E. Grammatikakis, E. Kyriakidis, K.D. Demadis, A.C. Diaz, L. Leon-Reina, Mineralogical characterization and firing temperature delineation on minoan pottery, focusing on the application of micro-Raman spectroscopy, *Heritage* 2 (2019) 2652–2664.
- [74] M. Thommes, et al., Physisorption of gases, with special reference to the evaluation of surface area and pore size distribution (IUPAC Technical Report), *Pure Appl. Chem.* 87 (2015) 1051–1069.
- [75] L.A.G. Aylmore, Q. J. The micropore size distribution of clay mineral systems, *J. Soil Sci.* 18 (1967) 1–17.
- [76] D.W. Rutherford, C.T. Chiou, D.D. Eberl, Effects of exchanged cation on the microporosity of montmorillonite, *Clay Clay Miner.* 45 (1997) 534–543.
- [77] D. Feng, et al., Water adsorption and its impact on the pore structure characteristics of shale clay, *Appl. Clay Sci.* 155 (2018) 126–138.